Scripta Materialia 234 (2023) 115562

Contents lists available at ScienceDirect

Scripta Materialia

journal homepage: www.journals.elsevier.com/scripta-materialia

Wedge disclination description of emergent core-shifted grain boundaries at free surfaces

Xiaopu Zhang *, Ipen Demirel, John J. Boland *

Centre for Research on Adaptive Nanostructures and Nanodevices (CRANN), AMBER SFI Research Centre and School of Chemistry, Trinity College Dublin, Dublin 2, Ireland

ARTICLE INFO

Keywords:
Grain boundaries
Surfaces
Emergent grain boundaries
Wedge disclination
Molecular statics simulation

ABSTRACT

Emergent grain boundaries at free surface control material properties such as nanomaterial strength, catalysis, and corrosion. Recently the restructuring of emergent boundaries on copper (111) surfaces was discovered experimentally and atomic calculations point to its universality in fcc metal systems. Restructuring is due to a preference for boundaries to shift their tilt axis across the $(1\bar{1}0)$ plane towards [112] and ultimately to form low energy [112] core shifted boundaries (CSBs). However, the observed geometry of these emergent boundaries is not reproduced by atomic calculations and the driving force is still controversial due to inconsistencies between the computational continuum analysis and atomic calculations. Here, using atomic calculations that involve a methodical shift of the dislocation core, we confirmed the geometry of emergent boundaries observed in experiment and reconciled the atomic calculations with the elastic analysis through the inclusion of a straight wedge disclination at the free surface.

The properties of emergent grain boundaries (eGBs) at free surfaces and other interfaces have attracted attention for more than half a century [1]. Intensive research has explored the effect of eGBs on growth and residual stress evolution in thin films and coatings [2–10], electrocatalytic phenomena such as CO_2 reduction [11,12], chemical catalysis [13], intergranular corrosion [14–16], and the mechanical properties of nanocrystalline materials [17,18]. In polycrystalline films of face-centered cubic metals, [111] textures are important and hence symmetrical tilt grain boundaries with [111] axis are common [19,20]. Symmetrical [111] tilt boundaries usually have two types of mean boundary planes $(1\bar{1}0)$ and $(11\bar{2})$ [21]. Recently, the restructuring of emergent boundaries with [111] tilt axis and $(1\bar{1}0)$ mean boundary planes in nanocrystalline copper films and macroscopic bicrystal copper samples with (111) surfaces was discovered experimentally [21,22]. High angle boundaries with [111] tilt axis and $(11\bar{2})$ mean boundary planes have been reported in electron microscopy analysis of the microscale polycrystalline copper films [23,24]. Although the restructuring phenomenon was initially reported for copper, simulations shows that this behavior is expected in all fcc metals [25].

Restructured eGBs observed in experiment involve the formation of axis shifted boundaries in which the original [111] tilt axis is shifted across the $(1\bar{1}0)$ plane towards [112], so the boundary cores lie in the low energy close packed $(11\bar{1})$ plane. This axis shift requires a commensurate out-of-plane rotation of the adjoining grains either side of the boundary and leads to the generation of elastic stresses in the triple junction region [21,22]. The energetics of eGB formation was analyzed by comparing continuum elastic modelling and atomic calculations, in an attempt to reproduce the observed eGB structure. To achieve this, computational continuum elastic analysis considered both the elastic anisotropy of the single crystalline material and elastic properties of polycrystals [21]. Only a small number of low-energy atomic structures were identified based on a cut-paste-shear-stitch method developed via a genetic algorithm and Monte-Carlo method [21]. The level of agreement and consistency between the two methods was limited, so that further analysis is necessary to lay a rigorous foundation for this approach. This analysis shows in a straightforward manner how the boundary energy reduction scales with the elimination of energetically-unfavorable boundary core facets [25].

In this paper, we introduce what we refer to as the core-shift method to systematically build, and to evaluate energetically restructured eGBs, instead of having to rely on a structure search. In this manner, it is possible to build all possible low energy core-shifted eGBs. We then analyzed the core structure of these calculated [112] core-shifted eGBs, uncovered the principles underlying our framework and demonstrated

* Corresponding authors.
E-mail addresses: xiaopuz@tcd.ie (X. Zhang), jboland@tcd.ie (J.J. Boland).

https://doi.org/10.1016/j.scriptamat.2023.115562
Received 23 February 2023; Received in revised form 20 April 2023; Accepted 12 May 2023
Available online 19 May 2023
1359-6462/© 2023 Acta Materialia Inc. Published by Elsevier Ltd. All rights reserved.

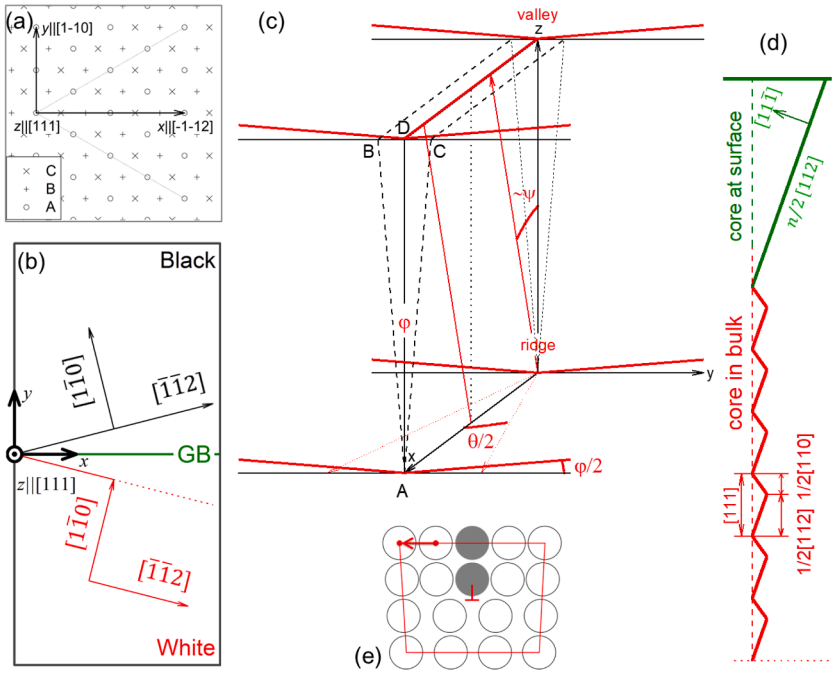

Fig. 1. Boundary geometry. (a) the median lattice adhering to the *xyz* coordination system. (b) bicrystals and their own coordination system are rotated $\pm\boldsymbol{\theta}/2$ along axis z or [111] of the median lattice. (c) out-of-plane rotation $\boldsymbol{\varphi}$, to shift the composite rotation axis $\boldsymbol{l}$. (d) [112] core-shifted boundary at top surface implied from experiment [21]. (e) core shift method illustrated with a pure edge dislocation in a single layer of the simple cubic lattice [27]. The grey atoms show the inserted atoms. Deleting the core atom or adding one atom below the core ⊥ shifts the dislocation line in this layer.

its wide applicability and consistency. Our analysis of the energetics of [112] core-shifted eGBs shows that eGBs at free surfaces are well described as a straight wedge disclination from the perspective of wedge geometry, the volume, the elastic stress and the surface stress.

The relationship between the in-plane boundary angle θ, shown in Fig. 1a-b, the out-of-plane rotation angle φ and the core shift angle (or inclination angle) ψ away from [111], shown in Fig. 1c, $\tan\psi = \tan(\varphi/2)/\sin(\theta/2)$ was verified experimentally for low angle [111] symmetrical tilt grain boundaries [22,26]. However, for boundaries with in-plane angles between ~ 15° to 30°, experiments point to a shift of the tilt axis from [111] to [112] close to the surface, while deep within the material the tilt axis is still [111] as shown in Fig. 1d [21]. This complex boundary structure involves a local symmetric rotation of the adjoining grains and is most appropriately described as a straight wedge disclination (Fig. 1c). At present there is no unified self-consistent description of [112] CSB formation that accounts for the depth

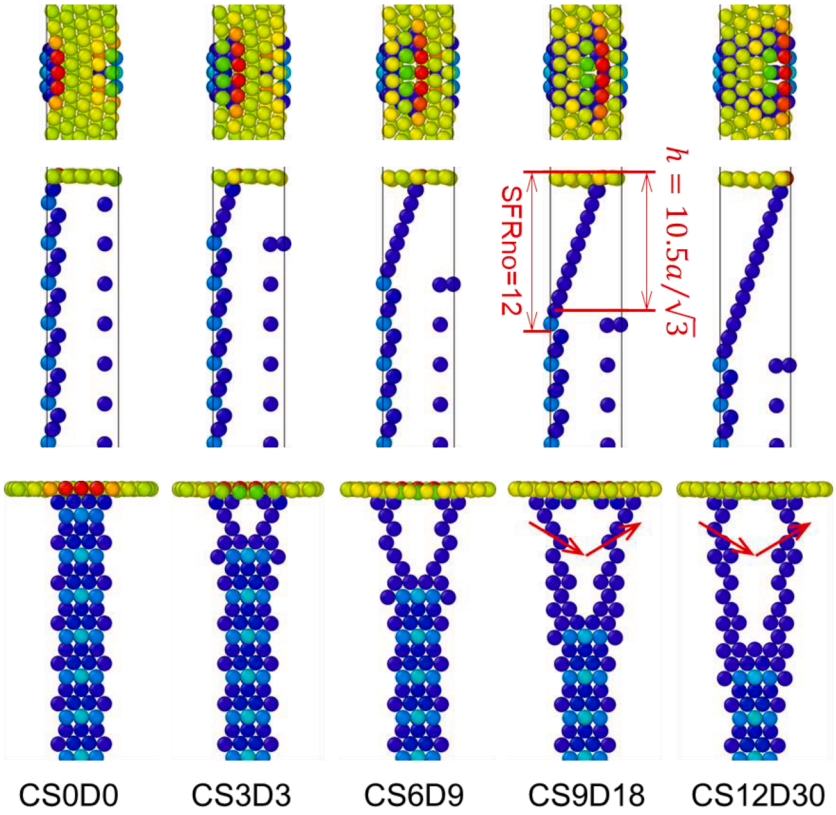

Fig. 2. Core-shift boundary with in-plane angle 13.17°. To shift the boundary core, we delete atoms at eGB in a step-by-step manner from the top surface. Core shift (CS) depth and total deleted atoms (D) are indicated. CS0D0 is the relaxed ideal eGB. After deleting one core atom each layer from the top 3 layers of CS0D0, we get CS3D3, whose stacking fault ribbon goes through 6 atoms layer from the top. After deleting one core atom each layer from the top 6 layers from CS3D3, we get CS6D9, whose stacking fault ribbon goes through 9 atoms layer from the top. The number of atomic layers in the stacking fault ribbon SFRno and the corresponding rotation depth $\boldsymbol{h}$ are shown in the middle panel for CS9D18. In the low panel for CS9D18 and CS12D30, the two partial dislocations are also shown.

dependence of the associated disclination.

To develop a systematic approach to model the energetics and depth of [112] CSB formation, we first consider the emergence of a single dislocation onto a surface (Fig. 1e). To shift the boundary core in each layer at the surface, deleting or inserting core atoms is necessary, as illustrated in Fig. 1e [27]. In the schematic shown, deleting one core atom shifts the local dislocation line upward in the boundary plane while adding one atom below the core atoms shift the local dislocation line downward. Both essentially involve movement of jogs along the boundary cores or jog nucleation and elimination, in contrast to dislocation climb which involves moving the dislocation lines [28–30]. Core atom deletion (insertion) creates valley (ridge) emergent boundaries, as described previously [21]. Using this approach, we developed a methodology to systematically evaluate the energetics at all stages in the core-shifting process, that keeps track of the number of atoms that are deleted or inserted and the formation of the associated wedge disclination.

The suspended films are built by stacking relaxed boundaries of ABC layers along [111] direction with the top layer C stacking, and adding an additional vacuum layer, as detailed in Fig. S1. The calculation methods used are described in the Supplementary Materials. The defect energy or the excess energy as a result of the presence of the interfaces, comprised of the top and bottom surfaces and two boundaries, and the four ideal eGBs [1,31] is $E_N = E_N^0 + \varepsilon_i$, where N is the total number of atoms in the system, the interfacial energy is $E_N^0 = 2\gamma_{gb}\cdot A_{gb} + 2\gamma_s\cdot A_s$, γ_{gb} is the boundary energy, γ_s the surface energy, A_{gb} the boundary area, A_s the surface area and ε_i the total energy of the four relaxed ideal eGBs in the calculated suspended films (see Fig. S1). The defect energy is calculated as $E_N = \sum_{i=1}^{N} e_i - Ne_{coh}$, where e_i and e_{coh} are atomic cohesive energy in the simulation system and in the bulk, respectively [21,22]. The ideal eGB refers to the boundary in which no atoms have been deleted or inserted. Taking the vacuum energy as the potential reference, the cohesive energy of a single copper atom is $e_{coh} = -3.54eV$ and the defect energy of the single vacancy in bulk is 1.27eV. Both values are consistent with earlier calculations [32].

Then we calculated the defect energy $E_{N-D} = (\sum_{i=1}^{N-D} e_i - (N-D)e_{coh})$ of suspended films, which includes a core-shifted eGB with D atoms deleted. The deleted atoms are added into the copper bulk while inserted atoms are taken from the copper bulk. In case of $D = 0$, the defect system is the same as the relaxed ideal eGB. Comparing the suspended films with relaxed ideal eGBs, the defect energy of the suspended film with a single core-shifted eGB includes the same surface energy, the same boundary energy, but a different eGB energy since any variation of the local surface energy or boundary energy is due to the presence of the triple junction itself. That is $E_{N-D} = E_N^0 + \varepsilon_{cs}$, where ε_{cs} is the energy of the one core-shifted eGB and 3 ideal eGBs (see Fig. S1). The defect energy variation

$$\Delta E \equiv E_{N-D} - E_N = \varepsilon_{cs} - \varepsilon_i = (\epsilon_{cse} - \epsilon_{ie})\cdot l_p \quad (1)$$

is the extensive energy difference between the core-shifted eGB energy ϵ_{cse} and the corresponding relaxed ideal eGB energy ϵ_{ie}, where l_p is the triple junction length along one period vector.

Fig. 2 shows the core shift process for an emergent grain boundary with in-plane angle θ =13.17° (eGB13.17). We find the boundary core by visualizing only high energy atoms of the calculated system in OVITO [33]. The top panel shows the top view, the middle panel the structure projected along the boundary normal, and the bottom panel the structure projected along the period vector. To shift the boundary core, we delete atoms step by step from the top surface layers of the eGB. The core shift (CS) depth and total deleted atoms (D) are indicated. CS0D0 is the relaxed ideal eGB with zero deleted atoms. After deleting one core atom from each of the top 3 layers of CS0D0, we get CS3D3, whose stacking fault ribbon (SFR) now extends 6 atom layers from the top. In this way, we removed one energetically-unfavorable segment $1/2[110]$ or jog along the boundary core [34] and hence the boundary energy is reduced. For low angle boundaries, the dislocation line then lies in a $(11\bar{1})$ plane and can dissociate into two partials with a stacking fault in-between (see CS9D18 & CS12D30 in Fig. 2) [22]. After deleting one

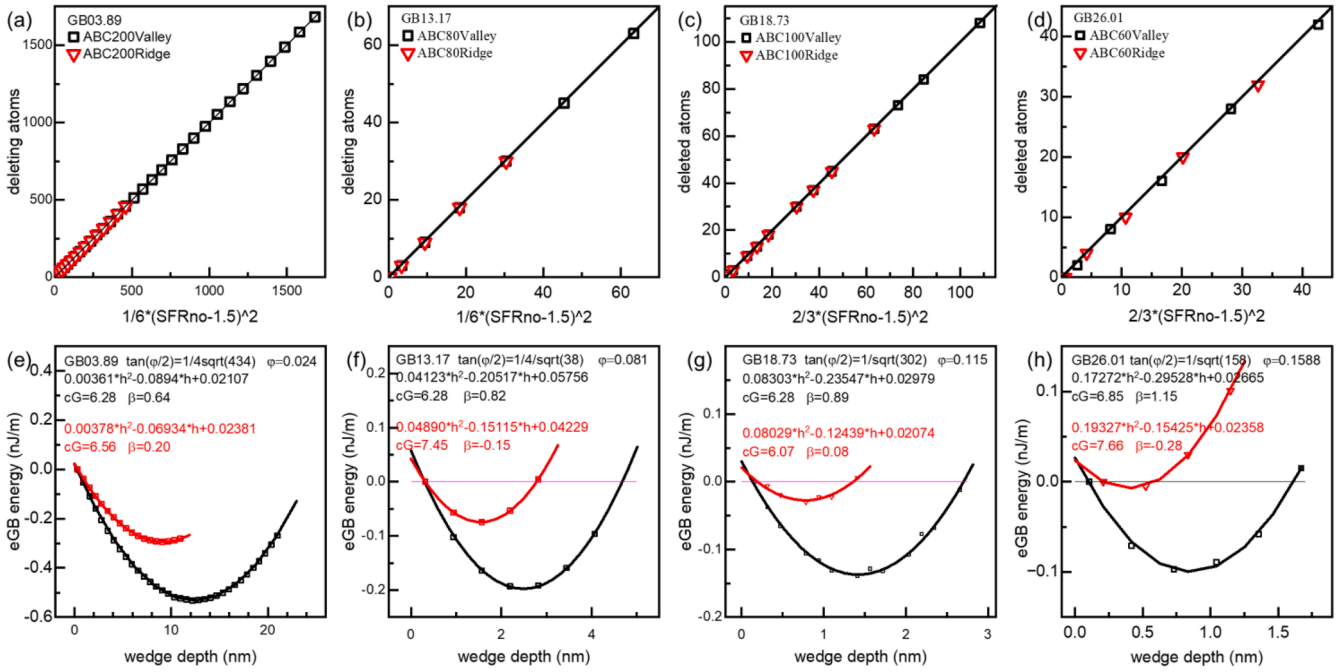

Fig. 3. Number of deleted atoms and core-shifted eGB energy. Upper panels (a-d) show the relationship between number of deleted atoms and effective depth from SFR thickness for representative eGBs with in-plane angle 3.89, 13.17, 18.73, 26.01. Lower panel (e-h) show dependence of eGB energies on wedge depth. Valley and ridge boundaries are shown as black and red curves, respectively. The fitting parameters to Eq. (3) are shown for each in-plane angle. The suspended film thickness used is shown - for the low energy boundary with in-plane angle 3.89, a thick suspended film with 200 ABC layer stacking or 600 total layers and nearly 10 million atoms was used. The coefficient $\boldsymbol{G}/(4\boldsymbol{\pi}(1-\boldsymbol{\nu}))$ and the surface stress are shown as cG and $\boldsymbol{\beta}$, respectively.

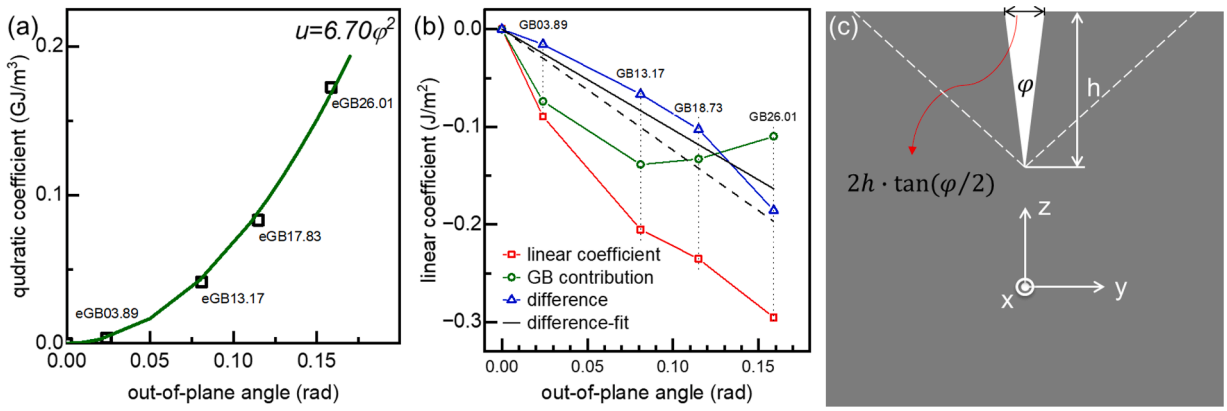

Fig. 4. Analysis of the quadratic & linear coefficients. (a) Dependence of the coefficient u of h^2 on out-of-plane angle. Data points are for eGB3.89, eGB13.17, eGB18.73 and eGB26.01. This plot demonstrates that the quadratic term of the defect energy is proportional to $\varphi^2 h^2$. (b) Plot of the linear term coefficient v, boundary term, the difference between previous two terms versus out-of-plane angle. The proportional fitting of the difference with constant ~ -1.03 is also shown. (c) Schematic show of one positive straight wedge disclination with the opening width $2h{\cdot}\tan(\varphi/2)$ at the free surface. The period vector pe_x points out of the paper and Frank vector for the wedge disclination is φe_x. The boundary normal is ne_y. The surface normal is le_z. The transition from the [111] boundary in bulk and the [112] CSB are schematically shown as the white dash line.

core atom from each of the top 6 layers of CS3D3, we get CS6D9, whose SFR extends 9 atom layers from the top and the total number of the deleted atoms is 9. Similarly, further deletion yields CS9D18 from CS6D9 and finally CS12D30 from CS9D18. The bottom panel clearly shows the emerging SFR as the number of deleted atoms is increased. Additional deletions continue to remove the energetically unfavorable boundary segments but increases the elastic energy contribution to the total energy, even though the boundary energy still decreases. The lower panel in Fig. 2 also shows that the SFR narrows when it meets the bulk boundary core and widens when it meets the free surface. In contrast, the emerging SFR at a ridge eGB becomes narrower when it meets both the bulk boundary core and the free surface (see Fig. S2). This predicted change in SFR width is consistent with earlier studies by electron microscopy, simulation, and surface technique [22,35-37].

To analyze the resulting core-shifted boundaries, we first determine the rotation depth h through which the adjoining grains have been rotated (see AD in Fig. 1c and green dash line in Fig. 1d), which is critical to accurately model the energy of systems containing a disclination. Since CSB formation involves grain rotation an incorrect depth gives the wrong coefficients for the quadratic terms for the bulk energy and consequently the wrong shear modulus (see below). Even a systematic offset in the depth gives a different linear term that is related to the interfacial energy contribution.

For each [112] CSB at the surface, the number of atomic layers in SFR is designated as *SFRno* in units of the atomic layer thickness. The number of layers that have been core shifted (CS) and from which atoms have been deleted is $SFRno - 3$, which is clearly seen in Fig. 2. The difference is related to the 3 layers at the transition between the bulk core and SFR core, which are in the SFR but not core shifted. During deletion or insertion of atoms, the corresponding eliminated volume or added volume per period vector length l_p is proportional to the volume variation $(SFRno - \alpha)^2 \cdot l_p$. To determine the appropriate scaling, we determined the numbers of deleted or inserted atoms as a function of the *SFRno* for four representative eGBs (eGB3.89, eGB13.17, eGB18.73 and eGB26.01). Since the number of deleted atoms D is in principle proportional to the volume, the best proportional fitting in Fig. S3 shows that $\alpha = 1.5$ for each grain boundary and hence the rotation depth is

$$h = (SFRno - 1.5)\cdot a \Big/ \sqrt{3} \tag{2}$$

where a is lattice constant and $a/\sqrt{3}$ the layer thickness. This can be understood by recognizing the [111] boundary core can be decomposed into a $1/2$[112] facet, which involve three atomic layers (Fig. 1d). When this facet connects with the eGB core, half of the length belongs to the bulk boundary core and the other half belongs to the emergent boundary core. For example, in CS9D18 the SFR depth *SFRno*, shown in Fig. 2, and core shifted depth from which the atoms are deleted are 12 and 9, respectively. Hence the rotation depth is 10.5 in unit of atomic layer thickness along [111], which corresponds to the rotation depth h of the wedge disclination associated with CS9D18.

Separately, we can calculate the volume of the wedge-shape disclination whose base is defined by the ABC vertices in Fig. 1c as $h^2 \cdot tan(\varphi/2) \cdot l_p = b \cdot a h^2/8$, where b is number of full dislocations $1/2[1\bar{1}0]$ per period vector. This volume divided by the single atom volume is the number of the deleted atoms per period. From this expression for the volume and Eq. (2), the calculated number of the deleted atoms per period for eGB03.89, eGB13.17 (both have a single core per period or $b = 1$) are $1/6 \cdot (SFRno - 1.5)^2$ and for eGB18.73 and eGB26.01 (that have four cores per period or $b = 4$) are $2/3 \cdot (SFRno - 1.5)^2$. The coefficient $1/6$ for eGB13.17 is consistent with the linear coefficient 0.1666 in Fig. S3. The result of this scaling analysis is shown in the top panel of Fig. 3(a-d) where all points plotted show an uncertainty of less than one atom. Note this scaling works equally for valley and ridge boundaries, where core atoms are deleted and added, respectively (see Fig. S1). Based on the depth analysis of the atomic structure, it is obvious that the volume variation for building core-shifted eGBs is well described by the wedge disclination.

The calculated defect energies for the four representative eGB structures as a function of the wedge depth are shown in the lower panels of Fig. 3(e-h). In each case, we kept the eGB period the same as the bulk boundaries and so we may miss some low energy eGB structures with long periods [38]. Each data point in the figure represents one core-shift [112] eGB structure. We find that the best way to fit the energy points at different depths in Fig. 3(e-h) is a parabolic equation [39, 40]. The intensive core-shifted eGB energy can be written as

$$\epsilon_{cse} - \epsilon_{ie} = u \cdot h^2 + v \cdot h + w \tag{3}$$

in units of J/m, where h is the rotation depth and u, v, w are coefficients to be determined. The fitting results for valley and ridge eGBs are shown in the graphs in the lower panels in Fig. 3(e-h) for each of the four representative in-plane angles θ. In all instances, the depth of the disclination wedge is larger for valley eGBs. The parabola shape is determined by coefficient u and the lateral position is determined by the ratio $-v/2u$. The vertical position is determined by coefficient w. The quadratic term and linear term correspond to the bulk energy and interfacial

energies, respectively [39,40]. The constant term corresponds to the energy variation of the linear defect and relates to the relaxed ideal eGB.

To understand the energy-depth dependence of the eGBs in Fig. 3(e-h), the contributions of the quadratic and linear terms to the defect energy of the core-shifted eGB were analyzed for each of the four representative in-plane angles θ. Fig. 4a shows the coefficient u of the quadratic term as a function of the corresponding out-of-plane angle φ given by $\tan\psi = \tan(\varphi/2)/\sin(\theta/2)$, with $\psi = 19.5^\circ$ for each [112] core-shifted eGB. We found that this coefficient u is proportional to φ^2 and hence the quadratic term is proportional to $\varphi^2 h^2$. This is consistent with finite element calculations in our previous paper [21]. The quadratic term has the form of the linear elastic energy of a straight wedge disclination $G/(4\pi(1-\nu))\cdot\varphi^2 h^2$, where G is shear modulus and ν Poisson's ratio, even though the discrete deletion or insertion of atoms cannot exactly describe a continuum wedge disclination [41–43]. Taking the Voigt average Poisson ratio $\nu = 0.324$ and the average coefficient 6.70 for $\varphi^2 h^2$ based on Fig. 4a yields a shear modulus of 56.9 GPa, which is close to the Voigt average value of 54.6 GPa shear modulus in polycrystals [28]. Alternatively, we fitted the energy-depth dependence to $\varphi^2 h^2$ for each valley eGB (see lower panel of Fig. 3, black curves), we find that the values of $G/(4\pi(1-\nu))$ are 6.28, 6.28, 6.28 and 6.85 corresponding to eGB3.89, eGB13.17, eGB18.73 and eGB26.01, respectively, which is consistent with an average value of 6.70. In summary, the quadratic coefficient is $u = G/(4\pi(1-\nu))\cdot\varphi^2$ and a direct measure of the materials elastic properties at their triple junctions.

To analyze the energy contributions to the interfacial linear terms in Fig. 3(e-h), we plot in Fig. 4b the coefficient v of the linear term (red curve) and the coefficient of the grain boundary energy (green curve) versus the out-of-plane angle φ for each valley eGB. The variation of the boundary energy per unit length along the period vector $-(\gamma_{gb[111]} - \gamma_{gb[112]}/\cos(\varphi/2))\cdot h \approx -(\gamma_{gb[111]} - \gamma_{gb[112]})\cdot h$ is a significant driver for CSB formation [21,34] but from Fig. 4b it makes an increasingly smaller contribution to the interfacial energy as both θ and φ increase. In fact, the difference between these two coefficients (blue curve) shows, particularly for low angle boundaries, a nearly linear dependence on φ, with a proportional constant β that has dimensions J/m^2. Hence the non-boundary contribution to the linear term per unit length along the period vector is $-\beta\varphi\cdot h$ or $-2\beta h\cdot\tan(\varphi/2)$ and depends on the wedge width $2h\cdot\tan(\varphi/2)$. We find that the value of β for our four representative eGBs are 0.64, 0.82, 0.89 and 1.17 J/m^2 and the linear fitting gave an average value of 1.03 J/m^2 (see the black solid line in Fig. 4c). These values are clearly different from the (111) surface energy 1.239 J/m^2 (plotted as the black dashed line in Fig. 4c) yet fall in the range of the reported values of the surface stress $0.7 \sim 1.3\ J/m^2$ [44]. As detailed in Tab. S2 the lowest energy eGB for each of our representative boundary has the wedge width of atomic scale dimensions is much smaller than the emergent SFR width and the groove width at the surface found in experiment and simulation. Therefore, the effect of the wedge disclination on the surface energy variation and the surface area variation can be modelled within the linear elastic approximation and the linear constant β is the effective surface stress in the system due to the formation of the local [112] CSB from the continuum wedge disclination.

In addition, we find that the effective surface stress at ridge eGBs is much smaller than that at valley eGBs. For ridge eGB13.17 and eGB26.01, the surface stress is negative and hence the triple junction is not stable and should spontaneously reorganize. Clearly additional experiment and simulation is needed to understand the non-boundary contribution to the linear term and the behavior of ridge eGBs. In summary, the coefficient for the linear term is $v = -(\gamma_{gb[111]} - \gamma_{gb[112]}/\cos(\varphi/2)) - 2\beta\cdot\tan(\varphi/2)$ and captures the boundary energy and effective surface stress contributions to [112] CSB formation.

In conclusion, we have shown that [112] core-shifted emergent boundaries are well described as a straight wedge disclination at the free surface. The subsurface geometry found is consistent with our previous geometrical analysis of experimental data. The determination of the SFR depth and in turn the depth of the disclination wedge is supported by our deleted atom and volume analysis. The results derived from an analysis of the quadratic and linear terms of the energy-depth relationship in Eq. (3) yield elastic parameters in bulk and surface stresses that are consistent with reported values.

The core shift method introduced here can be used as the starting point for research on other low energy structures beyond [112] wedge disclination. In this manner, it is possible to screen for the lowest energy structures that are consistent with experimental results, for example by fixing the CS depth and varying the out-of-plane angles through the insertion of jogs along the SFR. On this basis, the core shift method can also be used to calculate low energy structures at emergent metastable boundaries, to identify low energy structures in clusters and nanoparticles with dislocations, or to build subsurface metastable structures, and even to carry out structure searches at triple junctions in bulk.

J.J.B, X.Z. and I.D. acknowledge support from Science Foundation Ireland grants (12/RC/2278 and 16/IA/4462) and thank Trinity Centre for High Performance for providing the computing resource.

Declaration of Competing Interest

The authors declare that they have no known competing financial interests or personal relationships that could have appeared to influence the work reported in this paper.

Supplementary materials

Supplementary material associated with this article can be found, in the online version, at doi:10.1016/j.scriptamat.2023.115562.

References

[1] A.P. Sutton, R.W. Balluffi, Interfaces in Crystalline Materials, OUP, Oxford, 2006.
[2] W.D. Nix, B.M. Clemens, Crystallite coalescence: A mechanism for intrinsic tensile stresses in thin films, J Mater Res 14 (8) (1999) 3467–3473.
[3] E. Chason, A kinetic analysis of residual stress evolution in polycrystalline thin films, Thin Solid Films 526 (2012) 1–14.
[4] C. Friesen, C.V. Thompson, Comment on "Compressive stress in polycrystalline Volmer-Weber films", Phys Rev Lett 95 (22) (2005), 229601 author reply 229602.
[5] C. Friesen, C.V. Thompson, Correlation of stress and atomic-scale surface roughness evolution during intermittent homoepitaxial growth of (111)-oriented Ag and Cu, Phys Rev Lett 93 (5) (2004), 056104.
[6] C. Friesen, C.V. Thompson, Reversible stress relaxation during precoalescence interruptions of volmer-weber thin film growth, Phys Rev Lett 89 (12) (2002), 126103.
[7] J. Leib, R. Monig, C.V. Thompson, Direct evidence for effects of grain structure on reversible compressive deposition stresses in polycrystalline gold films, Phys Rev Lett 102 (25) (2009), 256101.
[8] R. Koch, D.Z. Hu, A.K. Das, Comment on "Compressive stress in polycrystalline Volmer-Weber films" - Reply, Phys Rev Lett 95 (22) (2005).
[9] R. Koch, D. Hu, A.K. Das, Compressive stress in polycrystalline volmer-weber films, Phys Rev Lett 94 (14) (2005), 146101.
[10] C.W. Pao, S.M. Foiles, E.B. Webb, D.J. Srolovitz, J.A. Floro, Thin film compressive stresses due to adatom insertion into grain boundaries, Phys Rev Lett 99 (3) (2007), 036102.
[11] R.G. Mariano, M. Kang, O.J. Wahab, I.J. McPherson, J.A. Rabinowitz, P.R. Unwin, M.W. Kanan, Microstructural origin of locally enhanced CO2 electroreduction activity on gold, Nat Mater 20 (7) (2021) 1000.
[12] R.G. Mariano, K. McKelvey, H.S. White, M.W. Kanan, Selective increase in CO2 electroreduction activity at grain-boundary surface terminations, Science 358 (6367) (2017) 1187–1192.
[13] X. Zhao, T.K. Gunji, F. Lv, B.L. Huang, R. Ding, J.G. Liu, M.C. Luo, Z.G. Zou, S. J. Guo, Direct Observation of Heterogeneous Surface Reactivity and Reconstruction on Terminations of Grain Boundaries of Platinum, Acs Mater Lett 3 (5) (2021) 622–629.
[14] D. An, T.A. Griffiths, P. Konijnenberg, S. Mandal, Z. Wang, S. Zaefferer, Correlating the five parameter grain boundary character distribution and the intergranular corrosion behaviour of a stainless steel using 3D orientation microscopy based on mechanical polishing serial sectioning, Acta Mater 156 (2018) 297–309.
[15] M. Bettayeb, V. Maurice, L.H. Klein, L. Lapeire, K. Verbeken, P. Marcus, Nanoscale Intergranular Corrosion and Relation with Grain Boundary Character as Studied In Situ on Copper, J Electrochem Soc 165 (11) (2018) C835–C841.
[16] E. Martinez-Lombardia, L. Lapeire, V. Maurice, I. De Graeve, K. Verbeken, L. H. Klein, L.A.I. Kestens, P. Marcus, H. Terryn, In situ scanning tunneling

microscopy study of the intergranular corrosion of copper, Electrochem Commun 41 (2014) 1–4.
[17] C. Wang, K. Du, K. Song, X. Ye, L. Qi, S. He, D. Tang, N. Lu, H. Jin, F. Li, H. Ye, Size-Dependent Grain-Boundary Structure with Improved Conductive and Mechanical Stabilities in Sub-10-nm Gold Crystals, Phys Rev Lett 120 (18) (2018), 186102.
[18] Y.-Y. Zhang, H. Xie, L.-Z. Liu, H.-J. Jin, Surface Triple Junctions Govern the Strength of a Nanoscale Solid, Phys Rev Lett 126 (23) (2021), 235501.
[19] H. Lee, S.D. Lopatin, The influence of barrier types on the microstructure and electromigration characteristics of electroplated copper, Thin Solid Films 492 (1-2) (2005) 279–284.
[20] D.B. Knorr, K.P. Rodbell, The role of texture in the electromigration behavior of pure aluminum lines, J Appl Phys 79 (5) (1996) 2409–2417.
[21] X. Zhang, M. Wang, H. Wang, M. Upmanyu, J.J. Boland, Restructuring of emergent grain boundaries at free surfaces – An interplay between core stabilization and elastic stress generation, Acta Mater 242 (2023), 118432.
[22] X. Zhang, J. Han, J.J. Plombon, A.P. Sutton, D.J. Srolovitz, J.J. Boland, Nanocrystalline copper films are never flat, Science 357 (6349) (2017) 397–400.
[23] T. Meiners, T. Frolov, R.E. Rudd, G. Dehm, C.H. Liebscher, Observations of grain-boundary phase transformations in an elemental metal, Nature 579 (7799) (2020) 375–378.
[24] L. Frommeyer, T. Brink, R. Freitas, T. Frolov, G. Dehm, C.H. Liebscher, Dual phase patterning during a congruent grain boundary phase transition in elemental copper, Nat Commun 13 (1) (2022) 3331.
[25] X. Zhang, J.J. Boland, Universal preference for low-energy core-shifted grain boundaries at the surfaces of fcc metals, Physical Review Research 5 (1) (2023), 013223.
[26] J. Schiotz, K.W. Jacobsen, Nanocrystalline metals: Roughness in flatland, Nat Mater 16 (11) (2017) 1059–1060.
[27] G.R. Love, Dislocation pipe diffusion, Acta Metallurgica 12 (6) (1964) 731–737.
[28] J.P. Hirth, J. Lothe, Theory of Dislocations, McGraw-Hill, 1982.
[29] N.F. Mott, The Mechanical Properties of Metals, P Phys Soc Lond B 64 (381) (1951), 729-&.
[30] S.F. Chu, P. Liu, Y. Zhang, X.D. Wang, S.X. Song, T. Zhu, Z. Zhang, X.D. Han, B. D. Sun, M.W. Chen, In situ atomic-scale observation of dislocation climb and grain boundary evolution in nanostructured metal, Nat Commun 13 (1) (2022).
[31] P. Muller, A. Saul, Elastic effects on surface physics, Surf Sci Rep 54 (5-8) (2004) 157–258.
[32] Y. Mishin, M.J. Mehl, D.A. Papaconstantopoulos, A.F. Voter, J.D. Kress, Structural stability and lattice defects in copper: Ab initio, tight-binding, and embedded-atom calculations, Phys Rev B 63 (22) (2001), 224106.
[33] A. Stukowski, Visualization and analysis of atomistic simulation data with OVITO-the Open Visualization Tool, Model Simul Mater Sc 18 (1) (2010), 015012.
[34] X. Zhang, J.J. Boland, Universal preference for low-energy core-shifted grain boundaries at the surfaces of fcc metals, Phys Rev Research 5 (2023).
[35] P.M. Hazzledine, H.P. Karnthaler, E. Wintner, Non-Parallel Dissociation of Dislocations in Thin Foils, Philos Mag 32 (1) (1975) 81–97.
[36] D. Rodney, G. Martin, Dislocation pinning by glissile interstitial loops in a nickel crystal: A molecular-dynamics study, Phys Rev B 61 (13) (2000) 8714–8725.
[37] J. Christiansen, K. Morgenstern, J. Schiotz, K.W. Jacobsen, K.F. Braun, K.H. Rieder, E. Laegsgaard, F. Besenbacher, Atomic-scale structure of dislocations revealed by scanning tunneling microscopy and molecular dynamics, Phys Rev Lett 88 (20) (2002), 206106.
[38] D.L. Olmsted, D. Buta, A. Adland, S.M. Foiles, M. Asta, A. Karma, Dislocation-pairing transitions in hot grain boundaries, Phys Rev Lett 106 (4) (2011), 046101.
[39] T. Radetic, F. Lancon, U. Dahmen, Chevron defect at the intersection of grain boundaries with free surfaces in Au, Phys Rev Lett 89 (8) (2002), 085502.
[40] T. Radetic, C. Ophus, D.L. Olmsted, M. Asta, U. Dahmen, Mechanism and dynamics of shrinking island grains in mazed bicrystal thin films of Au, Acta Mater 60 (20) (2012) 7051–7063.
[41] A.E. Romanov, A.L. Kolesnikova, Application of disclination concept to solid structures, Prog Mater Sci 54 (6) (2009) 740–769.
[42] A.E. Romanov, V.I. Vladimirov, Straight Wedge Disclination near a Free-Surface, Phys Status Solidi A 59 (2) (1980) K159–K163.
[43] A.E. Romanov, A.L. Kolesnikova, Elasticity Boundary-Value Problems for Straight Wedge Disclinations, A Review on Methods and Results, Reviews on Advanced Materials and Technologies 3 (2021) 55–95.
[44] C.W. Pao, D.J. Srolovitz, C.V. Thompson, Effects of surface defects on surface stress of Cu(001) and Cu(111), Phys Rev B 74 (15) (2006), 155437.